



# Enhanced catalytic ozonation inactivation of bioaerosols by $\text{MnO}_2/\text{Ni}$ foam with abundant oxygen vacancies and $\text{O}_3$ at atmospheric concentration

Haiyu Wang <sup>a,b</sup>, Linghui Peng <sup>a,b</sup>, Guiying Li <sup>a,b</sup>, Hongli Liu <sup>a,b</sup>, Zhishu Liang <sup>a,b</sup>, Huijun Zhao <sup>c</sup>, Taicheng An <sup>a,b,\*</sup>

<sup>a</sup> Guangdong-Hong Kong-Macao Joint Laboratory for Contaminants Exposure and Health, Guangdong Key Laboratory of Environmental Catalysis and Health Risk Control, Institute of Environmental Health and Pollution Control, Guangdong University of Technology, Guangzhou 510006, China

<sup>b</sup> Guangzhou Key Laboratory of Environmental Catalysis and Pollution Control, Guangdong Technology Research Center for Photocatalytic Technology Integration and Equipment Engineering, School of Environmental Science and Engineering, Guangdong University of Technology, Guangzhou 510006, China

<sup>c</sup> Centre for Clean Environment and Energy, Griffith School of Environment, Gold Coast Campus, Griffith University, Queensland 4222, Australia



## ARTICLE INFO

### Keywords:

Bioaerosol control technology  
Catalytic ozonation inactivation  
 $\text{MnO}_2/\text{Ni}$  foam  
Oxygen vacancies  
Reactive oxygen species

## ABSTRACT

Catalytic ozonation is a promising bioaerosol control technology, as  $\text{O}_3$  is prevalent in atmosphere. However,  $\text{O}_3$  at atmosphere concentration has limited oxidation potential and reactive oxygen species (ROSSs) production, leading incomplete bioaerosol inactivation. Therefore, a catalytic ozonation system with a manganese dioxide/Ni foam (MN) was prepared for efficient bioaerosol inactivation. The MN exhibited superior activity in catalytic ozonation bioaerosol inactivation, achieving 91.6% inactivation efficiency within 8.07 s at atmospheric concentration (0.1 ppm) of  $\text{O}_3$ . The inactivation efficiency can be further improved to 99.0% by regulating surface oxygen vacancies ( $\text{O}_v$ ) in MN, which is mainly attributed to abundant  $\text{O}_v$  of MN that facilitate rapid conversion of  $\text{O}_3$  to other ROSSs. Meanwhile, the mechanism of rapid bacterial inactivation was also clarified at cellular level, showing that ROSSs caused bacterial oxidative stress. This catalytic ozonation strategy would offer more choices to design efficient  $\text{O}_3$  catalysts for bioaerosol control and public health protection.

## 1. Introduction

Bioaerosols have become one of the major air pollutants in modern society [1–3]. Long-term exposure to bioaerosols can cause severe cardiovascular, respiratory, and cardiopulmonary diseases [4–6]. In addition, the fast spread of bioaerosols is responsible for the outbreaks of various major public health events including severe acute respiratory syndrome (SARS) [7], Ebola virus disease (EVD) [8], and severe acute respiratory syndrome coronavirus 2 (SARS-CoV-2) [9]. In this context, many technologies including chemical methods (e.g.,  $\text{ClO}_2$ ,  $\text{CH}_3\text{COOOH}$  [10,11], photocatalytic inactivation [12,13]) and physical methods [14–16] (e.g., filtration and electrostatic adsorption) have been adopted to bioaerosol control. However, these technologies show some drawbacks. Chemical spraying is toxic to human respiratory system when people occupied. Photocatalytic inactivation involves harmful UV light, while filtration and electrostatic may cause secondary contamination. Therefore, it is of great necessity to develop a bioaerosol control strategy that can realize highly efficient inactivation without harmful

byproducts.

Ozone ( $\text{O}_3$ ), with the advantages of no blind corners and no disinfection by-products, is very promising for the inactivation of bioaerosols [17], which is also prevalent in the environment with concentration of ~0.1 ppm at atmosphere [18].  $\text{O}_3$  inactivates bacteria mainly through oxidation by damaging the lipids of bacterial cell membranes, organelles, DNA, and RNA, which requires high concentrations due to limited oxidation potential of  $\text{O}_3$  (2.07 eV) [19–22]. Exposure of high concentrations of  $\text{O}_3$  is harmful to both humans and the environment [23,24], which cannot be applied to human occupied spaces [25]. On the other hand,  $\text{O}_3$  at atmosphere concentration has less reactive oxygen species (ROSSs) production, which may cause incomplete inactivation of bioaerosols and still pose a health exposure risk, thus inactivation efficiency of  $\text{O}_3$  at atmosphere concentration should be enhanced.

Catalytic ozonation technology ( $\text{O}_3$  oxidation in the presence of a catalyst) is an attractive option to enhance transformation of  $\text{O}_3$  into atomic oxygen and to further evolve into ROSSs for improving inactivation efficiency at the low concentration of  $\text{O}_3$  [26,27]. Greater oxidation

\* Corresponding author at: Guangdong-Hong Kong-Macao Joint Laboratory for Contaminants Exposure and Health, Guangdong Key Laboratory of Environmental Catalysis and Health Risk Control, Institute of Environmental Health and Pollution Control, Guangdong University of Technology, Guangzhou 510006, China.

E-mail address: [antc99@gdut.edu.cn](mailto:antc99@gdut.edu.cn) (T. An).

potential of ROSSs (e.g.  $\bullet\text{OH}$ , 2.78 eV) in catalytic ozonation endows it higher inactivation efficiency and the less  $\text{O}_3$  consumption [26]. To date, noble metal-containing catalysts such as Pd [28], Au [29], and Ag [30] are efficient catalysts for catalytic ozonation. However, the high cost and relative scarcity of noble metals limit the large-scale application of such catalysts. In this context, various non-noble metal  $\text{O}_3$  catalysts like earth-abundant transition metals and their oxides have been designed and synthesized [31]. Among them, manganese dioxide ( $\text{MnO}_2$ ) can be regarded as one of the most promising candidates due to its low cost and abundant on earth [32,33].  $\text{MnO}_2$  is always a reliable catalyst for efficient catalytic ozonation of odor methyl mercaptan [34] and bisphenol A [35]. In addition,  $\text{MnO}_2$  with oxygen vacancies ( $\text{O}_V$ ) is widely studied and applied for the ozone decomposition of volatile organic compound (VOC) ozonation [36,37], as  $\text{O}_V$  is considered to be the primary active site in the catalytic ozonation process.  $\text{O}_V$  in the  $\text{MnO}_2$  enhances transformation of  $\text{O}_3$  into atomic oxygen and further evolves into ROSSs for potentially improving inactivation efficiency. However, bulky  $\text{MnO}_2$  cannot be used for bioaerosol inactivation due to insufficient catalytic efficiency and easy fall off when exposed to the high air flow, resulting in catalysts loss [38]. Growing  $\text{MnO}_2$  on nickel foam (NF) seems to be a promising strategy, because NF can act as a support that providing desirable three-dimensional (3D) open-pore structures and high specific surface areas for  $\text{MnO}_2$  loading. Moreover, the 3D structure of NF also can be used as a microreactor to provide a space for sufficient contact between bioaerosols and ROSSs.

Thereby, this study aimed to construct the  $\text{MnO}_2$  sheets on nickel foam (MN) with abundant  $\text{O}_V$  for enhanced catalytic ozonation inactivation of bioaerosols and to understand the mechanisms involved in.  $\text{MnO}_2$  catalyst was anchored on the surface of NF via a simple hydrothermal reduction method. The bioaerosol inactivation efficiency of the MN catalytic ozonation at atmospheric concentration of  $\text{O}_3$  was investigated. Meanwhile, the catalytic mechanism was revealed by analyzing the phase compositions, surface chemical state, and redox abilities of MN. To illustrate deeply, the proposed inactivation mechanism was also verified at the cellular level by monitoring bacterial oxidative stress and membrane damage. This study may provide some basic information for the application of catalytic ozonation technology with low concentration of  $\text{O}_3$  in reducing the risk of bioaerosol exposure.

## 2. Experimental section

### 2.1. Materials and reagents

NF with thickness of 3.0 mm was purchased from Guangzhou Lige Technology Co., LTD.  $(\text{NH}_4)_2\text{C}_2\text{O}_4$  ( $\geq 99\%$ ),  $\text{KMnO}_4$  ( $\geq 99\%$ ), HCl (36% – 38%),  $\text{CH}_3\text{COOH}$  ( $\geq 99.5\%$ ),  $\text{CH}_3\text{COCH}_3$  ( $\geq 99.5\%$ ), nutrient broth, and nutrient agar were purchased from Aladdin Co. Ltd. DCFH-DA fluorescent probe was purchased from Beyotime Biotechnology Co. Ltd. All chemicals and reagents were used as received without any treatment.

### 2.2. Catalyst synthesis and characterization

**Synthesis of MN:** MN was prepared by a simple one-step hydrothermal reduction method. Firstly, NF pieces of  $2.5\text{ cm} \times 2.5\text{ cm}$  were successively immersed in an ultrasonic bath of  $\text{CH}_3\text{COCH}_3$ , 1 M HCl, and deionized  $\text{H}_2\text{O}$  for 30 min to remove stains and surface oxides, respectively. Then, the cleaned NF was quickly placed in a 100 mL Teflon-lined autoclave. Secondly, a mixed solution of 0.2 mM  $\text{KMnO}_4$  and 0.1 mM  $(\text{NH}_4)_2\text{C}_2\text{O}_4$  in 80 mL deionized  $\text{H}_2\text{O}$  was slowly added into the autoclave. After 15 min of ultrasonic mixing, the Teflon-lined autoclave was transferred into an oven at  $180^\circ\text{C}$  for 12 h. Finally, the obtained  $\text{MnO}_2/\text{NF}$  (denoted as MN) was washed with deionized  $\text{H}_2\text{O}$  to remove soluble Mn salts, and dried at  $60^\circ\text{C}$  for 12 h.

**Synthesis of  $\text{MNE}_x$ :**  $\text{MNE}_x$  samples were prepared by hydrothermal treatment of MN different concentration of ethanol solution ranging

from 0% – 50%. In detail, the MN obtained from hydrothermal treatment was then quickly placed in a 100 mL Teflon liner containing 80 mL different concentration of ethanol. The reaction temperature and time were  $130^\circ\text{C}$  and 12 h, respectively. The obtained samples (denoted as  $\text{MNE}_0$ ,  $\text{MNE}_{0.25}$  and  $\text{MNE}_{0.5}$ ) were dried at  $60^\circ\text{C}$  for 24 h.

**Characterization:** Scanning electron microscopy (SEM) observations were performed on Hitachi S-3400 N at an accelerating voltage of 5 kV. Transmission electron microscopy (TEM) images were obtained by JEOL JEM-2100 microscope at an accelerating voltage of 200 kV. The surface morphology of the sample was measured by an atomic force microscopy (AFM) (Bruker Dimension Icon). The crystalline structure of the samples was characterized by an X-ray diffractometer (XRD) (Rigaku Ultima IV) using Cu-K $\alpha$  radiation. Raman spectra of the samples were obtained by Laser Micro-Raman Spectrometer (Horiba Scientific-LabRAM HR evolution, 514 nm laser). X-ray photoelectron spectroscopy (XPS) (Thermo Fisher ESCALAB 250Xi) was used to evaluate the bonding environment and oxidation state of surface elements (ca. 10 nm) on the catalysts. The formula used to estimate the average oxidation state (AOS) is  $\text{AOS} = 8.956 - 1.126 \Delta E$  ( $\Delta E$  is the difference in the binding energy between two peaks) [39]. The generated  $\bullet\text{OH}$ ,  $\bullet\text{O}_2$  and  $^1\text{O}_2$  were detected by electron paramagnetic resonance (EPR) spectrometer (Bruker A-300, www.ece-shi.com). 5,5-dimethyl-1-pyrroline N-oxide (DMPO) and 2,2,6,6-tetramethyl-4- 112 piperidinol (TEMP) were used as the spin trapping reagents. In detail, 0.1 g catalysts were dispersed in a 100 mM DMPO/TEMP solution (2 mL) and then  $\text{O}_3$  (0.1 ppm) was purged for 10 min. Finally, catalysts were filtered and the solvent was  $\text{H}_2\text{O}$  trapping  $\bullet\text{OH}$  and  $^1\text{O}_2$  and dimethyl sulfoxide (DMSO) for  $\bullet\text{O}_2$ . The ROSSs generated on the catalysts in air were estimated by chemiluminescence. Luminol (100  $\mu\text{M}$ ) was employed as the indicator. Firstly, MN catalyst was exposed to  $\text{O}_3$  flow for 10 min (catalytic  $\text{O}_3$  reaction). After that, 100  $\mu\text{L}$  luminol was dropped on the surface of the catalysts, immediately. The chemiluminescence of the luminol was detected by microplate reader (Varioskan LUX, ThermoFisher, USA) at the same time.

### 2.3. Catalytic ozonation bioaerosol inactivation experiment

**Bioaerosol generation:** Firstly, the experimental strain *E. coli* DH5 $\alpha$  was inoculated in a Luria-Bertani (LB) broth at  $37^\circ\text{C}$ . After about 12 h of shaking incubation, a bacterial suspension with a concentration of approximately  $10^9 \text{ CFU mL}^{-1}$  was obtained. Then, the above bacterial suspension was centrifuged at 8000 rpm for 2 min and resuspended in 0.9% NaCl solution. After washing twice with 0.9% NaCl solution, the above bacterial suspension was poured in a Collison six-jet nebulizer (BGI Inc., Waltham, MA) for bioaerosol generation. Then, the bioaerosols were injected and balanced in a chamber with a volume of 50 L. The concentration of bioaerosols was adjusted by the concentration of bacterial stock suspension. The particle size of generated bioaerosols is approximately 1 – 3  $\mu\text{m}$  (Fig. S1).

**Bioaerosol sampling:** In this study, liquid sampler and an Anderson six-stage sampler were used to collect the bioaerosols from the reactor. The sampling medium of liquid sampler was 10 mL of 0.9% NaCl solution. The sampling flow rate of the liquid sampler was  $7 - 12.5 \text{ L min}^{-1}$ . The sampling flow rate of the Anderson six-stage sampler was  $28.3 \text{ L min}^{-1}$ . The sampling air volume was adjusted to 50 L. The collected samples (100  $\mu\text{L}$ ) were diluted and cultured on a nutrient agar plate at  $37^\circ\text{C}$  for 18 – 24 h.

#### 2.3.1. Evaluation of bioaerosol inactivation performance of MN catalytic ozonation

The experimental setup for bioaerosol inactivation by MN catalytic ozonation was shown in Fig. S2. In detail, the MN was sealed in the middle of the quartz reactor, which connected to the outlet of the balance chamber. An  $\text{O}_3$  generator (FQ-160, Beyok, China) was used to generate  $\text{O}_3$  at a concentration of 0.1 ppm, 1 ppm, and 5 ppm. During the inactivation reaction, the bioaerosols and  $\text{O}_3$  passed through the MN from the top to the bottom of the quartz reactor. At last, the bioaerosols

were collected by the bioaerosol sampler from the outlet of the quartz reactor. Meanwhile, the concentration of  $O_3$  in the reactor was monitored online using a  $O_3$  sensor (RS485, Vemsee, China). The detailed parameters of the bioaerosol inactivation experiment were shown in Table S1. The inactivation efficiency ( $\eta$ ) was calculated using the following Eq. 1:

$$\eta = \left( 1 - \frac{C}{C_0} \right) \quad (1)$$

$C_0$  ( $CFU\ m^{-3}$ ) is the concentration of initial bioaerosols;  $C$  ( $CFU\ m^{-3}$ ) is the concentration of bioaerosols after catalytic ozonation inactivation.

#### 2.4. Cellular assay

**Bacterial oxidative stress response:** Bacterial oxidative stress response was monitored by the fluorescent probe DCFH-DA (Beyotime Biotechnology), and the detailed operation is shown in the [Supporting information \(SI\)](#).

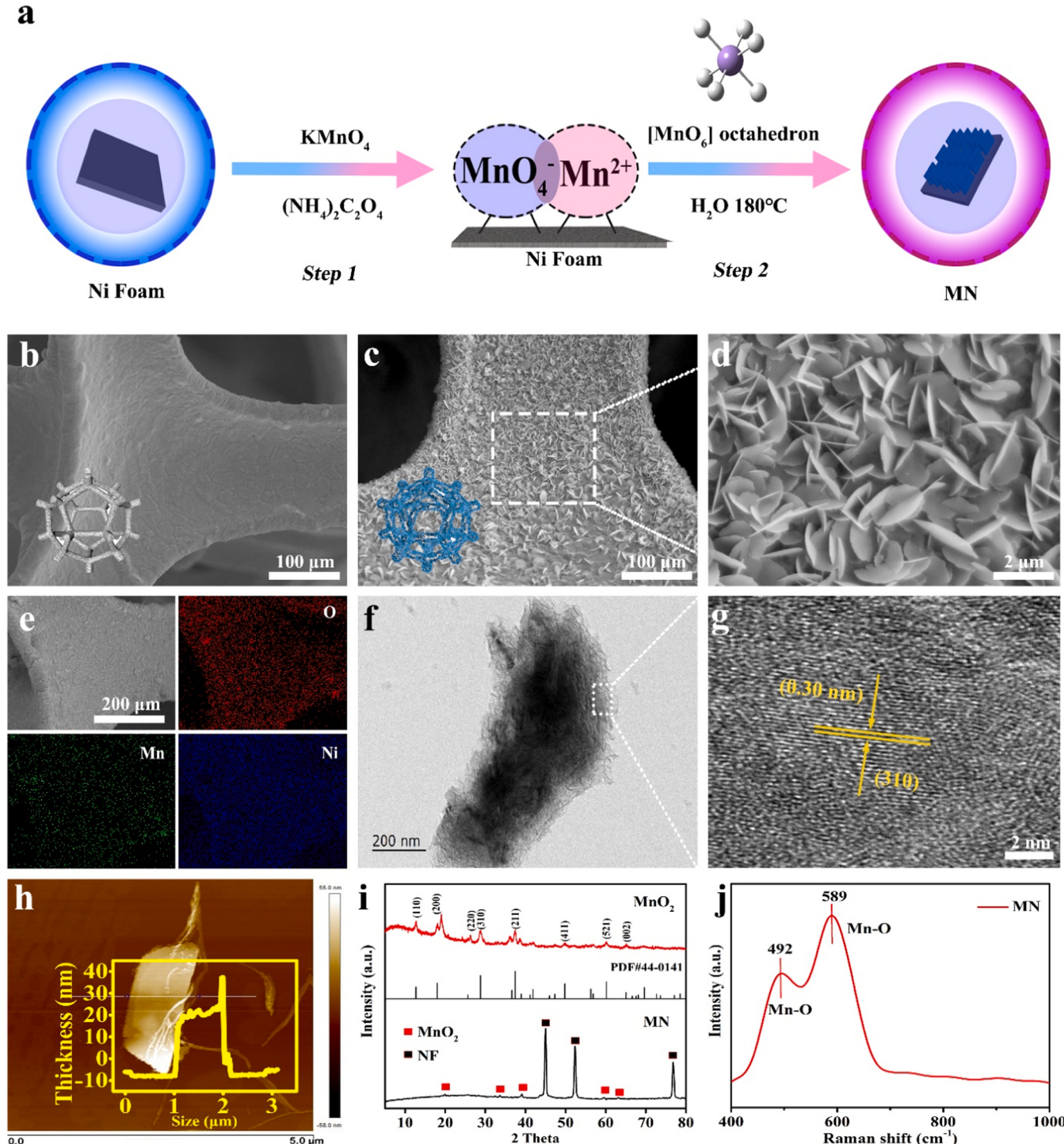


**Fig. 1.** a) Illustration of synthesis procedure of  $MnO_2$  onto NF. SEM images of b) bare NF, MN c) at low magnification and d) at high magnification; e) EDS elemental mapping images of MN; TEM images of MN f) at low magnification and g) at high magnification; h) AFM images of MN; i) XRD patterns of MN and  $MnO_2$  powder, and j) Raman patterns of MN.

**Bacterial adenosine triphosphate:** The adenosine triphosphate (ATP) was measured using a detection kit (Beyotime Biotechnology, China), and the detailed operation is shown in SI.

**Bacterial morphology:** The morphology of the bacteria was observed by SEM at an accelerating voltage of 5 kV. The detailed preparation steps of SEM samples are also provided in SI.

### 3. Results and discussion

#### 3.1. Morphology and structure characterization of MN

The synthesis process of  $\text{MnO}_2$  on the surface of NF by a facile hydrothermal treatment is schematically illustrated in Fig. 1a.  $\text{KMnO}_4$  undergoes a redox reaction with  $(\text{NH}_4)_2\text{C}_2\text{O}_4$  solution to form  $\text{MnO}_2$  at 180 °C. The chemical reactions can be formulated as two reactions:  $2\text{MnO}_4^- + 5\text{C}_2\text{O}_4^{2-} + 16\text{H}^+ = 10\text{CO}_2\uparrow + 2\text{Mn}^{2+} + 8\text{H}_2\text{O}$  (1);  $2\text{MnO}_4^- + 3\text{Mn}^{2+} + 2\text{H}_2\text{O} = 4\text{H}^+ + 5\text{MnO}_2\downarrow$  (2) [40]. When the clean NF is immersed in the mixture of  $(\text{NH}_4)_2\text{C}_2\text{O}_4$  and  $\text{KMnO}_4$  solution, the  $[\text{MnO}_6]$  octahedron unit (the basic structural units for  $\text{MnO}_2$ ) is firstly formed on the surface of NF by bonding with oxygen atoms of oxygen-containing functional groups via electrostatic force. In the subsequent hydrothermal process, the  $[\text{MnO}_6]$  octahedron unit grows into  $\text{MnO}_2$  on the surface of NF.

The morphology and microstructure of MN were systematically analyzed. The SEM images in Fig. 1c shows that the  $\text{MnO}_2$  was successfully anchored onto the smooth surface of the NF (Fig. 1b) after 12 h of hydrothermal treatment. The SEM image at high magnification (Fig. 1d) and energy-dispersive X-ray (EDS) mapping (Fig. 1e) of MN also confirm successful and uniform growth of  $\text{MnO}_2$  nanosheets onto NF. The microstructure of the  $\text{MnO}_2$  sample was further observed via peeling  $\text{MnO}_2$  nanosheets from the surface of NF, showing square-sheet shape with size of 2  $\mu\text{m}$  (Fig. 1f). The detailed analysis of HRTEM images (Fig. 1g) reveals that the lattice space of  $\text{MnO}_2$  nanosheets is 0.30 nm,

corresponding to the (310) plane of  $\text{MnO}_2$ . In addition, the AFM image indicates that the  $\text{MnO}_2$  nanosheets anchored onto the surface of NF are very thin and the thickness is only about 20 nm (Fig. 1h). XRD pattern of  $\text{MnO}_2$  peeling from NF displayed in Fig. 1i shows distinct peaks at 12.8°, 18.1°, 25.7°, 28.9°, 37.6°, 49.9°, 60.2°, and 65.1°, corresponding to the diffraction plane of (110), (200), (220), (310), (211), (411), (521), and (002), respectively (PDF 44 – 0141) [34]. The peaks of MN located at 44.9°, 52.3° and 76.7° could be ascribed to the (111), (200), and (220) planes of Ni foam (PDF# 04–0850) [41]. The molecular arrangement structure of MN also analyzed by a Raman spectrometer (Fig. 1j). Two peaks located at 492 and 589  $\text{cm}^{-1}$  are derived from the stretching vibration of the Mn-O bond in  $[\text{MnO}_6]$  sheet basal planes and the Mn-O symmetric stretching vibration along the direction perpendicular to  $[\text{MnO}_6]$  groups [42,43]. In short, the above characterization results verify the successful growth of sheet-like  $\text{MnO}_2$  onto the surface of NF.

#### 3.2. Evaluation of catalytic ozonation inactivation efficiency of bioaerosols onto prepared catalyst

The MN catalyst was assembled in a quartz reactor for catalytic ozonation bioaerosol inactivation tests. The bioaerosol inactivation efficiency was estimated by the standard plate counting method of bacteria. In order to obtain convective bioaerosol inactivation efficiency in catalytic ozonation system of  $\text{MN}/\text{O}_3$ , the inactivation performance of  $\text{O}_3$ , NF,  $\text{O}_3/\text{NF}$ , MN, and  $\text{MN}/\text{O}_3$  systems were comparatively investigated. Here, 0.1 ppm concentration of  $\text{O}_3$  (an average atmospheric concentration) was chosen for catalytic ozonation reaction. As displayed in Fig. 2a, the bioaerosol inactivation efficiency of  $\text{O}_3$  alone (0.1 ppm) is only 1.9% at the retention time of 8.07 s, indicating that at an atmospheric concentration of  $\text{O}_3$  is not able to significantly inactivate bacteria in such a short time. Meanwhile, the similar low bioaerosol inactivation efficiency of only 9.8% with NF alone was found, suggesting that the NF is not effective in removing bioaerosols, either. For  $\text{NF}/\text{O}_3$

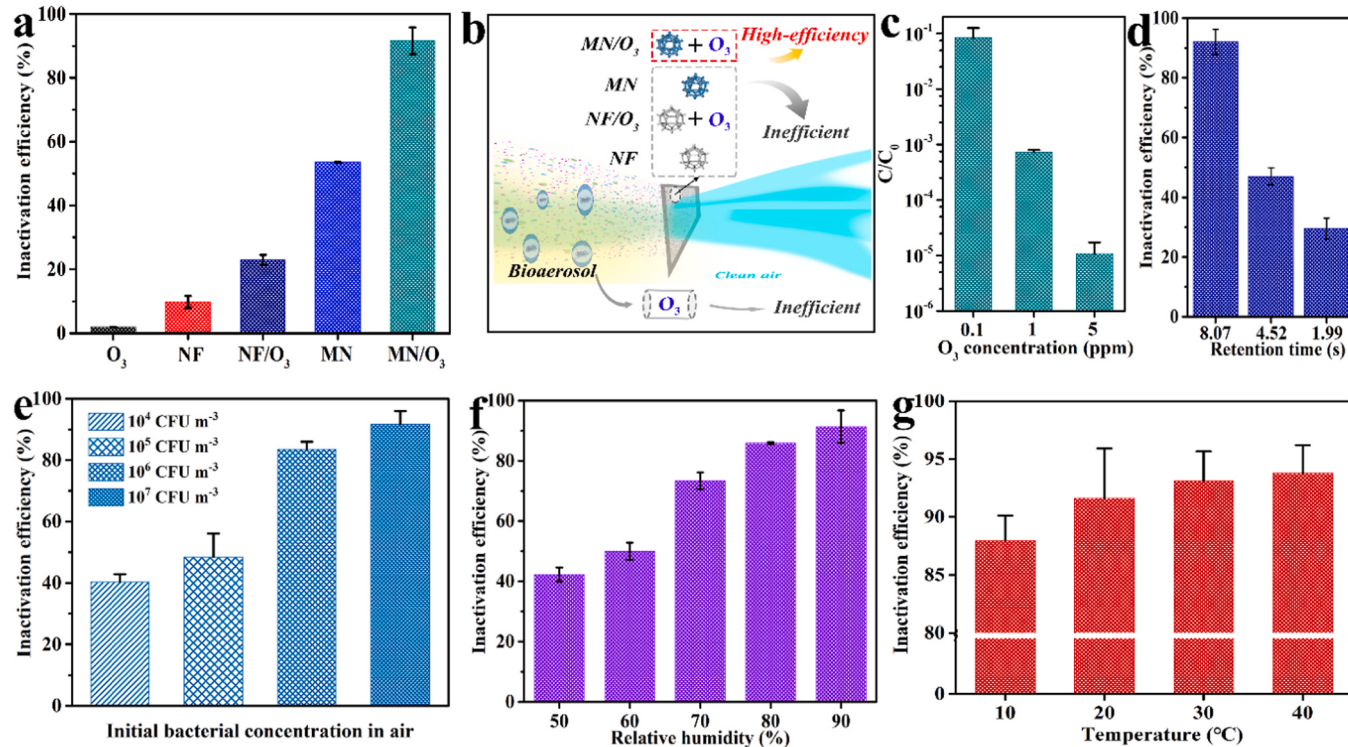


**Fig. 2.** a) Comparison of the bioaerosol inactivation efficiency of  $\text{O}_3$ , NF,  $\text{NF}/\text{O}_3$ , MN, and  $\text{MN}/\text{O}_3$  (RH = 90%, retention time = 8.07 s), respectively; b) Illustration of the bioaerosol inactivation efficiency of  $\text{O}_3$ , NF,  $\text{NF}/\text{O}_3$ , MN, and  $\text{MN}/\text{O}_3$ , respectively; c) Effect of concentration of  $\text{O}_3$  on the bioaerosol inactivation efficiency. d) Effect of retention time on bioaerosol inactivation efficiency (RH = 90%). e) Effect of concentration of bacteria on bioaerosol inactivation efficiency; f) Effect of relative humidity on bioaerosol inactivation efficiency (retention time = 8.07 s); g) Effect of temperature on bioaerosol inactivation efficiency.

and MN systems, the bioaerosol inactivation efficiency were also obtained as 22.9% and 53.6%, respectively. MN catalyst shows higher inactivation efficiency than NF/O<sub>3</sub>, which can partly inactivate a portion of bioaerosols. However, in MN/O<sub>3</sub> system, the inactivation efficiency of bioaerosols is obtained as 91.6%, which is much higher than that of O<sub>3</sub>, NF/O<sub>3</sub> and MN. As illustrated in Fig. 2b, the inactivation efficiency of MN/O<sub>3</sub> system is significantly higher than other three systems, maybe attributed to that MnO<sub>2</sub> can catalyze O<sub>3</sub> at an atmospheric concentration (0.1 ppm) to produce high oxidation potential of ROSs and some physical damages by MnO<sub>2</sub> nanosheets for bioaerosol inactivation at a short time [44]. In MN system without O<sub>3</sub>, no catalytic oxidation involved, the limited inactivation efficiency of bioaerosols may attribute to physical damage by MnO<sub>2</sub> nanosheets, based on our previous study [41]. Furthermore, the low inactivation efficiency of NF/O<sub>3</sub> probably owns to lacks of not only catalytic oxidation but also physical damage. Even though O<sub>3</sub> possesses oxidation potential to inactivate bioaerosols, the efficiency of it is limited at such a low concentration and short retention time. However, in the MN/O<sub>3</sub> system, enhanced catalytic oxidation was achieved by reaction between MN catalyst and O<sub>3</sub>, resulting in high inactivation efficiency of bioaerosols.

In order to explore the performance of the MN/O<sub>3</sub> system for practical application, the impacts of concentration of O<sub>3</sub>, retention time, concentration of bioaerosols, environmental temperature and relative humidity on the catalytic ozonation inactivation efficiency of bioaerosols in MN/O<sub>3</sub> system were investigated. Firstly, increasing the concentration of O<sub>3</sub> can significantly improve bioaerosol inactivation efficiency of the MN/O<sub>3</sub> system. With the concentration of O<sub>3</sub> increases from 0.1 to 1 and then to 5.0 ppm, the bacteria reduction improves significantly (from 1 log to  $\sim$ 2 log and then to 4 log) (Fig. 2c). These results highlight the excellent catalytic ozonation performance of MN to some extent to O<sub>3</sub> even at atmospheric concentrations (0.1 ppm). However, the usage of high concentration of O<sub>3</sub> (1 and 5 ppm) to inactivate indoor bacteria is still in debate, because exposure of high concentrations of O<sub>3</sub> is harmful to both humans and the environment [45]. Thus, to balance the catalytic ozonation inactivation efficiency with O<sub>3</sub> exposure risks for catalytic ozonation inactivation of bioaerosols in the enclosed spaces, 0.1 ppm of O<sub>3</sub> was therefore selected for the following MN/O<sub>3</sub> catalytic inactivation experiments.

The retention time is of great importance in the practical application of this efficient technology. As plotted in Fig. 2d, the long retention time has positive influence on the catalytic ozonation inactivation efficiency of bioaerosols. The inactivation efficiency is only 29.5% at a short retention time of 1.99 s, and then increases to 47.1% at a retention time of 4.52 s. With the retention time extended to 8.07 s, the inactivation efficiency of bioaerosols reaches up to 91.6%. The high inactivation efficiency at long retention time can be easily explained by the fact that bioaerosols have more chances to interact with produced ROSs, yielding the improved inactivation efficiency. However, it does not mean an endless extension of the retention time for increasing inactivation efficiency, because long residence time causes the slow flow rates, resulting in low processing capacity per unit time (Table S1). The purification air volume and catalytic inactivation efficiency need to be reasonably balanced, thus an optimized retention time of 8.07 s was chosen in the following tests.

In atmospheric environment conditions, the concentration of bioaerosols varies greatly in different areas, ranging from  $\sim$ 10<sup>3</sup> to  $\sim$ 10<sup>6</sup> CFU m<sup>-3</sup> [46–48]. Therefore, the catalytic ozonation inactivation efficiency of MN/O<sub>3</sub> system under different initial concentrations of bioaerosols (10<sup>7</sup>, 10<sup>6</sup>, 10<sup>5</sup>, and 10<sup>4</sup> CFU m<sup>-3</sup>) was also explored. As depicted in Fig. 2e, the inactivation efficiency of bioaerosols obtained about 40.2% at concentration of 10<sup>4</sup> CFU m<sup>-3</sup>. With the concentration of bioaerosols further increases from 10<sup>5</sup> to 10<sup>6</sup> CFU m<sup>-3</sup>, the inactivation efficiency improves from 48.4% to 83.5% and then reaches 91.6% at 10<sup>7</sup> CFU m<sup>-3</sup>. It can be explained by that the holes size of NF (200–300  $\mu$ m) is obviously larger than the particle size of generated bioaerosols (1–3  $\mu$ m), such a structure makes it easy for bioaerosols to pass through

the holes of the NF with the airflow. When the concentration of bioaerosols increased, more cells approach the NF surface, which in turn are attacked by the ROSs generated on the surface of the catalyst, thus the inactivation efficiency was improved [49].

Furthermore, the catalytic ozonation inactivation efficiency of bioaerosols in MN/O<sub>3</sub> system was further measured under different relative humidity (RH) conditions. As presented in Fig. 2f, the inactivation efficiency is obtained as only 42.2% when the RH is 50%  $\pm$  3%, then increases to 50.1% and 73.4% at 60%  $\pm$  3% RH and 70%  $\pm$  3% RH, respectively. When the RH continuously increase to 80%  $\pm$  3%, the inactivation efficiency rises to 85.8% accordingly. The reason maybe that MN could catalyze the reaction of O<sub>3</sub> and OH<sup>-</sup> in water vapors to produce H<sub>2</sub>O<sub>2</sub> and then H<sub>2</sub>O<sub>2</sub> is further converted to ROSs at high RH [50]. Thus, the high concentration of ROSs enhances the bioaerosol inactivation performance of MnO<sub>2</sub>/O<sub>3</sub> at high RH. In addition, the cell membrane of bacteria may swell and become thin in high RH, resulting in easy inactivation of the bacteria [45]. These results show that the inactivation efficiency of bioaerosols in the MN/O<sub>3</sub> system is positively correlated with RH, indicating that the MN/O<sub>3</sub> system can adapt to humid environment for bioaerosol control.

Additionally, the inactivation efficiency of bioaerosols in MN/O<sub>3</sub> system at various ambient temperatures was also studied. It can be seen from Fig. 2g that the inactivation efficiency rises slowly with increase of ambient temperature. At low temperature (10  $\pm$  5 °C), the inactivation efficiency is obtained as 87.9%, while reaches 91.6%–93.1% at the near standard ambient temperature range (20  $\pm$  5 °C–30  $\pm$  5 °C). As the temperature rises to 40  $\pm$  5 °C, the inactivation efficiency increases to 93.7%. The reason maybe that high temperature causes the quick mass transfer of O<sub>3</sub> molecules during catalytic ozonation reactions [36]. All above results confirm that the MN/O<sub>3</sub> system possesses a high potential to bioaerosol control at different environmental conditions for practical applications.

### 3.3. Catalytic ozonation inactivation mechanism of bioaerosols

#### 3.3.1. Exploration of the promoting effect of oxygen vacancies (O<sub>V</sub>) and ROSs

To understand the underlying mechanisms of the high catalytic ozonation inactivation activity, the element valence states of MN surface were investigated [43]. The valence state of Mn element can influence the formation of O<sub>V</sub> on MnO<sub>2</sub> to maintain charge balance and O<sub>V</sub> always works as active site in the catalytic ozonation process [51]. To explore the promotion of O<sub>V</sub> in catalytic ozonation inactivation activity, the surface features and the valence state of Mn element in MN after the reduction by different concentration of ethanol (introducing O<sub>V</sub> in MnO<sub>2</sub>, which leads to reduction of valence state of Mn element) were first analyzed. It can be seen from Fig. S3 that the Mn element valence state of MN changed significantly after being reduced by ethanol (MNE<sub>0.5</sub>) and used for catalytic ozonation (used MNE<sub>0.5</sub>). Mn 2p3/2 spectrum of MN can be divided into three peaks located at 640.6, 641.6, and 642.9 eV, which are corresponding to Mn<sup>2+</sup>, Mn<sup>3+</sup>, and Mn<sup>4+</sup>, respectively [52]. Peak area represents the percentage of different Mn element valence states. Existing low valance states (Mn<sup>2+</sup> and Mn<sup>3+</sup>) of Mn indicates the formation of O<sub>V</sub> [53]. The percentages of Mn<sup>2+</sup> and Mn<sup>3+</sup> increased while the percentage of Mn<sup>4+</sup> decreased in MNE<sub>0.5</sub> after ethanol treatment, indicating that the valence state of the MNE<sub>0.5</sub> reduced and the amount of O<sub>V</sub> increased. On the other hand, the percentages of Mn<sup>2+</sup> and Mn<sup>3+</sup> decreased while Mn<sup>4+</sup> increased significantly in used MNE<sub>0.5</sub>, which maybe due to the oxidation of Mn element by O<sub>3</sub> and occupation of O<sub>V</sub> by absorbates. The AOS of surface Mn element is further estimated by the binding energy difference ( $\Delta E$ ) between the two peaks of Mn 3 s (Fig. 3a). The calculated AOS for Mn element of MN is 3.32, and the Mn elements AOS of MNE<sub>0.5</sub> is 2.65, indicating the Mn element valence state was decreased after ethanol reduction. However, the Mn elements AOS of used MNE<sub>0.5</sub> increased to 3.10. These results fully manifest that the surface elements valence

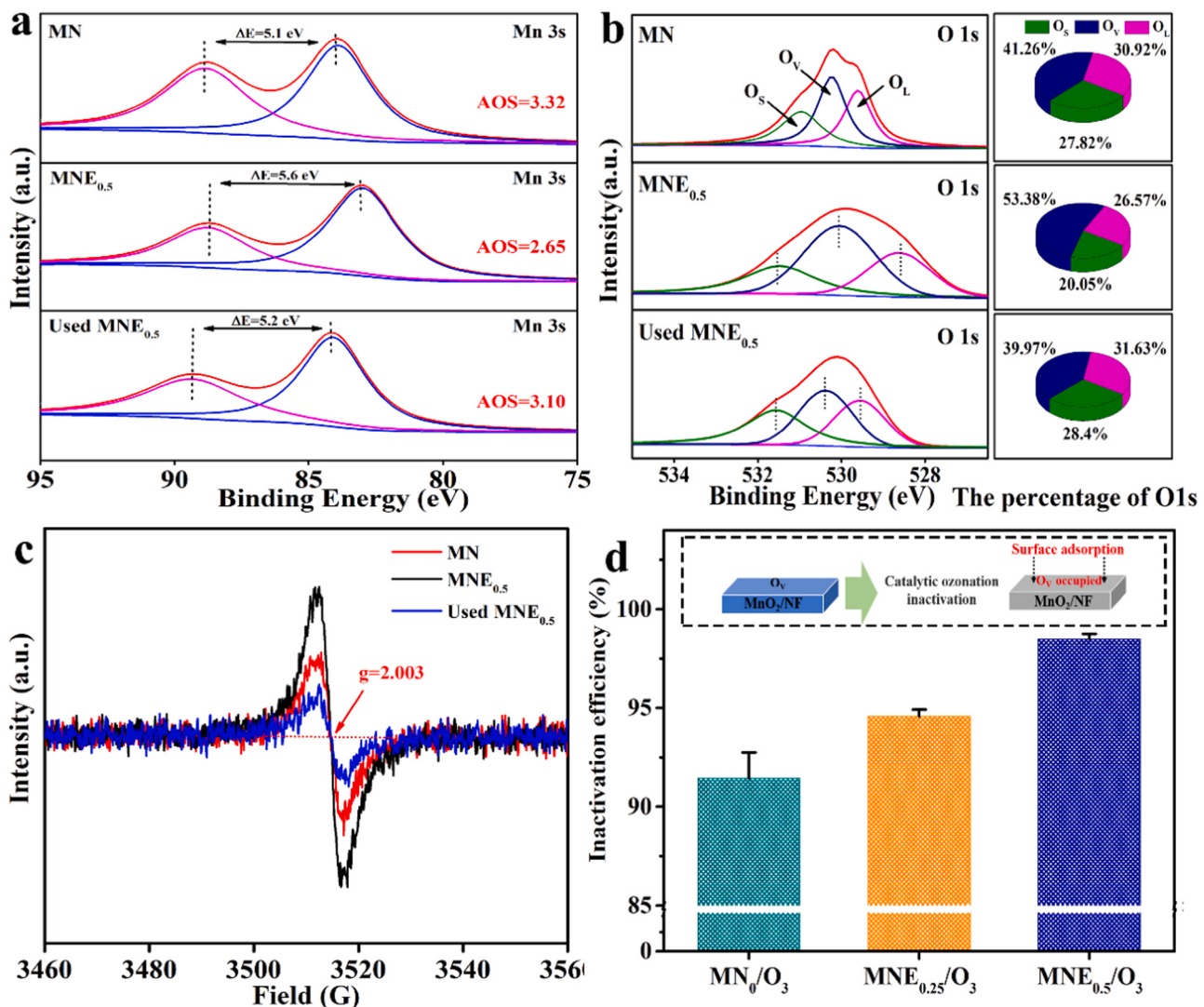


**Fig. 3.** XPS spectra of a) Mn 3 s and b) O 1 s of MN, MNE<sub>0.5</sub> and used MNE<sub>0.5</sub>; c) EPR spectra of MN, MNE<sub>0.5</sub> and used MNE<sub>0.5</sub>; d) Comparison of the bioaerosol inactivation efficiency of MN<sub>0</sub>/O<sub>3</sub>, MNE<sub>0.25</sub>/O<sub>3</sub> and MNE<sub>0.5</sub>/O<sub>3</sub> (RH = 90%, retention time = 8.07 s).

states of MN reduced afterethanol reduction and increased after catalytic ozonation reaction, indicating O<sub>v</sub> in the MN was consumed after catalytic ozonation reaction.

To figure out if O<sub>v</sub> is the key factor in catalytic ozonation inactivation efficiency, the O 1 s spectra of the catalysts were analyzed immediately thereafter. The O 1 s spectrum of MN in Fig. 3b is divided into three peaks located at 529.9, 531.5, and 533.3 eV, which are assigned to the lattice oxygen species (O<sub>l</sub>), low-coordinated oxygen adsorbed in oxygen vacancies (O<sub>v</sub>) such as O<sup>2-</sup>, O<sup>2-</sup>, OH groups and surface residual hydroxyl molecules (O<sub>s</sub>), respectively [54,55]. It is worth noting that the percentage of various oxygen species in MNE<sub>0.5</sub> and used MNE<sub>0.5</sub> are both changed obviously compare with MN. In particular, the percentage of O<sub>v</sub> increases from 41.3% (MN) to 53.4% (MNE<sub>0.5</sub>), which demonstrates that ethanol reduction method significantly increased the concentration of surface O<sub>v</sub>. On the contrary, the percentage of O<sub>v</sub> in used MNE<sub>0.5</sub> decreases to 40.0%, which may cause by O<sub>v</sub> occupation by surface adsorbates [56]. The high O<sub>v</sub> concentration in MN was further verified by the EPR results (Fig. 3c), where the symmetric signal with a g-value at 2.003 contributed to the electrons trapped in the O<sub>v</sub> [34]. In addition, the higher peak intensity means the higher concentration of the O<sub>v</sub> in the catalyst. The peak intensity of MNE<sub>0.5</sub> was higher than that of MN and used MNE<sub>0.5</sub>, verifying that MNE<sub>0.5</sub> has the highest concentration of O<sub>v</sub> among the three catalysts, which is also consistent with the

XPS results. Moreover, survey spectra of MN, MNE<sub>0.5</sub> and used MNE<sub>0.5</sub> were also demonstrated in Fig. S4, indicating that the element composition of elements on the surface of the catalyst did not change before and after catalytic ozonation. In short, the above results indicate that the abundant surface O<sub>v</sub> in MN is the active site in the catalytic ozonation process.

To explore the promoting effect of O<sub>v</sub> in catalytic ozonation inactivation activity, the catalytic ozonation inactivation efficiency of MN after ethanol reduction were also evaluated. As displayed in Fig. 3d, the catalytic ozonation inactivation efficiency of MNE<sub>0</sub>/O<sub>3</sub> MNE<sub>0.25</sub>/O<sub>3</sub> and MNE<sub>0.5</sub>/O<sub>3</sub> were obtained as 92.0%, 94.6% and 99.0%, respectively, indicating that the catalytic ozonation inactivation efficiency increased with rise of O<sub>v</sub> concentration in MN. Moreover, we also investigated the cycling test of MN/O<sub>3</sub> system. As shown in Fig. S5, the bioaerosol inactivation of MN/O<sub>3</sub> system gradually decreased for 4 times, which may be that the adsorbed H<sub>2</sub>O molecule is hard to desorb from the surface O<sub>v</sub>. Importantly, the morphology (Fig. S6), element components (Fig. S7) and structural features (Figs. S8 and S9) of MNE<sub>0.5</sub> are similar to that of MN. Moreover, Figs. S10 and 2i show that XRD pattern of MNE<sub>0.5</sub> powder is corresponding to MnOOH/MnO<sub>2</sub> heterojunction, indicating that some of the valence of Mn (+4) in MnO<sub>2</sub> has been reduced to Mn (+2). It was reported that the formation of heterojunction also contributes to the increase of O<sub>v</sub> on the catalyst [57]. Consequently,

we can confirm that the key factor of the high catalytic ozonation inactivation activity of  $\text{MN}/\text{O}_3$  system is the abundant  $\text{O}_\text{V}$  on the surface of  $\text{MN}$ .

$\text{O}_\text{V}$  is beneficial to electron transfer to participate in the catalytic ozonation reaction and produce more ROSSs such as  $\bullet\text{OH}$ ,  $\bullet\text{O}_2^-$  and  $^1\text{O}_2$ , which is critical for highly inactivation activity [58]. To confirm it, the ROSSs ( $\bullet\text{OH}$ ,  $\bullet\text{O}_2^-$  and  $^1\text{O}_2$ ) generation in catalytic ozonation was detected in liquid phase by EPR spectrometer. As shown in Fig. 4a, the characteristic peaks of  $\bullet\text{OH}$  with the intensity of 1: 2: 2: 1 can be detected in all samples, while shows a higher intensity in  $\text{MNE}_{0.5}/\text{O}_3$  system than that of  $\text{MN}/\text{O}_3$  and used  $\text{MNE}_{0.5}/\text{O}_3$  systems, indicating higher concentration of ROSSs generation in  $\text{MNE}_{0.5}/\text{O}_3$  system. This result indicates that  $\text{MNE}_{0.5}/\text{O}_3$  possesses a stronger capability to generate  $\bullet\text{OH}$  than other systems, which attributes to the low valence state of Mn in  $\text{MNE}_{0.5}$  system. Meanwhile, as shown in Figs. 4b and 4c, the concentration of  $\bullet\text{O}_2^-$  and  $^1\text{O}_2$  in  $\text{MNE}_{0.5}/\text{O}_3$  system were also higher than that of  $\text{MN}/\text{O}_3$  system, while dropped significantly after being used. Moreover, we also detected the ROSSs generated in air by chemiluminescence of luminol to confirm the results from EPR. As previously reported, luminol (100  $\mu\text{M}$ ) was employed as the indicator to reflect the generation of ROSSs by chemiluminescence [59,60]. When luminol reacts with ROSSs, it can generate blue fluorescence ( $\sim 420 \text{ nm}$ ), which can be used to signal the generation of ROSSs by the  $\text{MN}/\text{O}_3$  system. Firstly,  $\text{MN}$  catalyst was exposed to  $\text{O}_3$  flow for 10 min (catalytic  $\text{O}_3$  reaction). After that, 100  $\mu\text{L}$  luminol was dropped on the surface of the catalysts, immediately. The chemiluminescence of the luminol was detected by microplate reader at

the same time. We found that the characteristic peak at 420 nm of the  $\text{MNE}_{0.5}$  was the highest among  $\text{MN}$ ,  $\text{MNE}_{0.5}$  and used  $\text{MNE}_{0.5}$  systems (Fig. 4d), indicating that the ROSSs generation in  $\text{MNE}_{0.5}$  is the highest. These results not only confirm that ROSSs were generated at the interface of the catalyst and air, but also show that the concentrations of ROSSs are corresponding to the EPR results in the different systems. Therefore, we can firstly conclude that abundant  $\text{O}_\text{V}$  is beneficial to generate ROSSs to inactivate bioaerosols.

In this study, we found that the  $\text{O}_\text{V}$  concentration in the  $\text{MnO}_2$  catalyst has impacts on the performance of bioaerosol inactivation, which supported the oxygen vacancies theory among many theories (Table S2). Therefore, the possible mechanism of the ROSSs generated from  $\text{O}_\text{V}$  in the  $\text{MN}/\text{O}_3$  system could be summarized together with early references by the following reaction pathways [61–63]. Firstly, in the  $\text{MN}/\text{O}_3$  system,  $\text{O}_3$  can be captured by the  $\text{O}_\text{V}$  onto the surface of  $\text{MN}$  when  $\text{O}_3$  go through  $\text{MN}$ . The  $\text{O}_\text{V}$  onto  $\text{MnO}_2$  transfers two electrons to an oxygen atom of  $\text{O}_3$  (two-electron donor), resulting in one  $\text{O}_2$  molecule desorbing into the ambient air and one reactive oxygen ( $\text{O}_2^-$ ) remaining in the  $\text{O}_\text{V}$  (Eq. 2). Secondly, the other  $\text{O}_3$  molecule can then react with the  $\text{O}_2^-$  in  $\text{O}_\text{V}$  to produce one  $\text{O}_2$  molecule and a bridging  $\text{O}_2$  dimer (peroxide,  $\text{O}_2^{2-}$ ) species (Eq. 3). At last, charge transfer interactions drive the reaction between  $\text{O}_2^-/\text{O}_2^{2-}$  and  $\text{O}_3$  to generate ROSSs such as  $\bullet\text{OH}$ ,  $\bullet\text{O}_2^-$  and  $^1\text{O}_2$  (Eq. 4 and Eq. 5). Simultaneously, to sustain the electrostatic balance, the  $\text{O}_2^-$  accumulated on surface of  $\text{MN}$  can be converted into  $\text{O}_2$  molecules, releasing a part of  $\text{O}_\text{V}$  (Eq. 6).

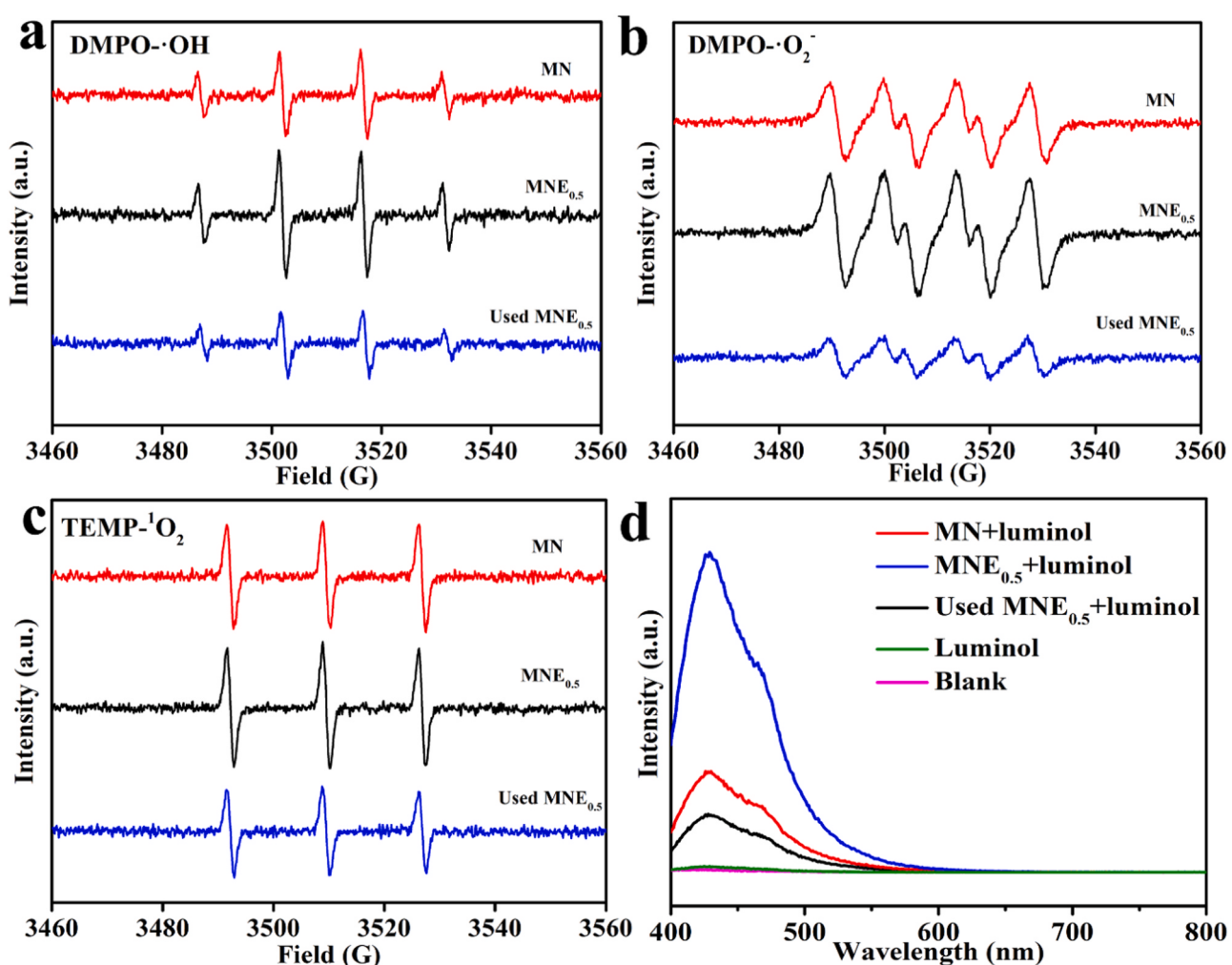
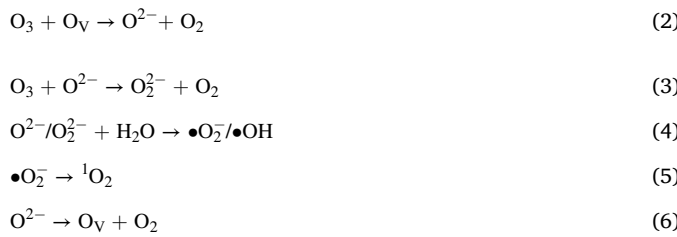


Fig. 4. Comparison of EPR spectra of  $\text{MN}$ ,  $\text{MNE}_{0.5}$  and used  $\text{MNE}_{0.5}$ . a)  $\bullet\text{OH}$ , b)  $\bullet\text{O}_2^-$  and c)  $^1\text{O}_2$ ; d) Chemiluminescence spectra of luminol dropping on  $\text{MN}$ ,  $\text{MNE}_{0.5}$  and used  $\text{MNE}_{0.5}$ .



Although there is lack of data support for the generation of atomic oxygen ( $\text{O}^-/\text{O}^{2-}$ ) in the activation pathway of  $\text{O}_3$ , it also can be considered that the exposure of more active sites ( $\text{O}_V$ ) on the MN promotes the production of ROSSs in the catalytic ozonation process, and thus improves the inactivation activity of bacteria in bioaerosols.

### 3.3.2. Exploration of the bacterial oxidative stress and damage in the MN/ $\text{O}_3$ system

In order to further understand the mechanism of the bacteria inactivation, the oxidative stress and morphology change of bacteria in the MN/ $\text{O}_3$  system were investigated. The oxidative stress is a self-defense response of bacteria when they suffer from external stimulation and one of the indicators of bacterial oxidative stress is intracellular ROSSs production [64]. As displayed in Fig. 5a, the intracellular ROSSs level of bacteria being treated in MN/ $\text{O}_3$  system is much higher than that of control system. This result indicates catalytic ozonation in the MN/ $\text{O}_3$  system can induce significant increase of intracellular ROSSs levels of bacteria. Severe oxidative stress of bacteria may cause a decrease in cellular activity, which can be indicated by the ATP activity of bacteria. ATP activity of bacteria being treated in MN/ $\text{O}_3$  is much lower than that of without treatment, indicating that severe oxidative stress of bacteria caused by MN/ $\text{O}_3$  system reduce cellular activity obviously. Further, we found that morphology of bacteria changed after being treated in the MN/ $\text{O}_3$  system. As shown in Fig. 5b and c, the morphology of bacteria treated in the MN/ $\text{O}_3$  system was collapsed and shrunken, while that of untreated bacteria was complete with rod shape, indicating the damage of cell membrane of bacteria in the MN/ $\text{O}_3$  system. The inset picture of the Fig. 5b and c also show that the number of culturable bacteria in bioaerosols reduced significantly after being treating in the MN/ $\text{O}_3$  system. These results correspond to the results of oxidative stress and cellular activity of bacteria. Therefore, the bacteria in bioaerosols were under severe oxidative stress in the MN/ $\text{O}_3$  system, leading to reducing cellular activity, further cell membrane damage and cell inactivation in the end. It is worth noting that this severe oxidative stress response of bacteria comes from the external stimuli of high concentration of ROSSs generated in the MN/ $\text{O}_3$  system. In this situation, not only intracellular ROSSs from oxidative stress, but also extracellular ROSSs from catalytic ozonation attack bacteria to destroy membrane structure and bacterial normal metabolic processes, yielding inactivation of them. It can be concluded that the high bioaerosol inactivation efficiency of the MN/ $\text{O}_3$  system attributes to the tremendous structural and physiologic damages

of bacteria.

### 3.3.3. Proposed inactivation mechanisms of the MN/ $\text{O}_3$ system

Hence, based on the results discussed above, the bioaerosol inactivation mechanism of the MN/ $\text{O}_3$  system was proposed. As shown in Fig. 6,  $\text{O}_3$  molecules (atmospheric concentration) are firstly captured by the  $\text{O}_V$  (active sites) on the surface of MN catalyst ( $\text{MnO}_2$  with abundant  $\text{O}_V$  were anchored on NF). The  $\text{O}_V$  transfers two electrons to  $\text{O}_3$ , generating ROSSs such as  $\bullet\text{OH}$ ,  $\bullet\text{O}^{2-}$  and  $^1\text{O}_2$  in air. When the bacteria approaching the surface of MN, they can be attacked by the high concentration of ROSSs. The bacteria will be under severe oxidative stress response to this external stimulate, yielding reduction of ATP activity. Finally, the intracellular ROSSs that caused by oxidative stress and ROSSs generated in the MN/ $\text{O}_3$  system can synergistically destroy bacterial membrane structure and normal metabolic processes of the bacteria, leading to inactivation of them. Therefore, in the MN/ $\text{O}_3$  system,  $\text{O}_V$  on the  $\text{MnO}_2$  catalyzes low concentration of  $\text{O}_3$  to highly active ROSSs, yielding high bioaerosol inactivation efficiency within a short time.

## 4. Conclusions

The limitations of  $\text{O}_3$  oxidation for bioaerosol inactivation are that the potential toxicity to humans at high concentrations, but poor efficiency at low concentrations owing to the limited oxidation potential. In this study, a novel catalytic ozonation strategy consisting of a MN catalyst coupled with  $\text{O}_3$  was successfully proposed. The catalyst with abundant exposed active sites ( $\text{O}_V$ ) exhibited an outstanding bioaerosol inactivation activity of 99.0% at 0.1 ppm of  $\text{O}_3$  (atmospheric concentration). The MN catalyst with abundant  $\text{O}_V$  can convert low concentrations of  $\text{O}_3$  into ROSSs with high oxidation capacity to rapidly inactivate bioaerosols. Bacteria suffered from severe bacterial oxidative stress, cellular activity decrease and membrane damage in the MN/ $\text{O}_3$  system, yielding quick inactivation of bioaerosols. This work offers a highly efficient catalytic ozonation strategy for inactivation of bioaerosols, which can be a promising candidate for comprehensive and deep air purification in home, schools, vehicles, etc.

## CRediT authorship contribution statement

**Li Guiying:** Writing – review & editing, Funding acquisition. **Liu Hongli:** Visualization, Investigation. **Liang Zhishu:** Validation, Methodology. **Zhao Huijun:** Validation. **Wang Haiyu:** Writing – original draft, Methodology, Formal analysis. **Peng Linghui:** Methodology, Data curation. **An Taicheng:** Supervision, Funding acquisition, Conceptualization.

## Declaration of Competing Interest

The authors declare that they have no known competing financial interests or personal relationships that could have appeared to influence

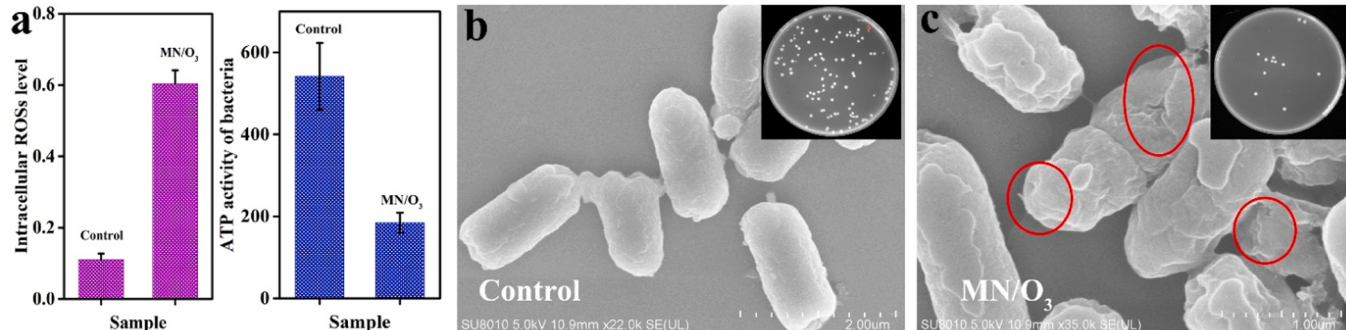


**Fig. 5.** a) The intracellular ROSSs and ATP of bacteria without and after being inactivated with MN/ $\text{O}_3$ ; SEM images of bacteria after being inactivated b) without, and c) with MN/ $\text{O}_3$ .

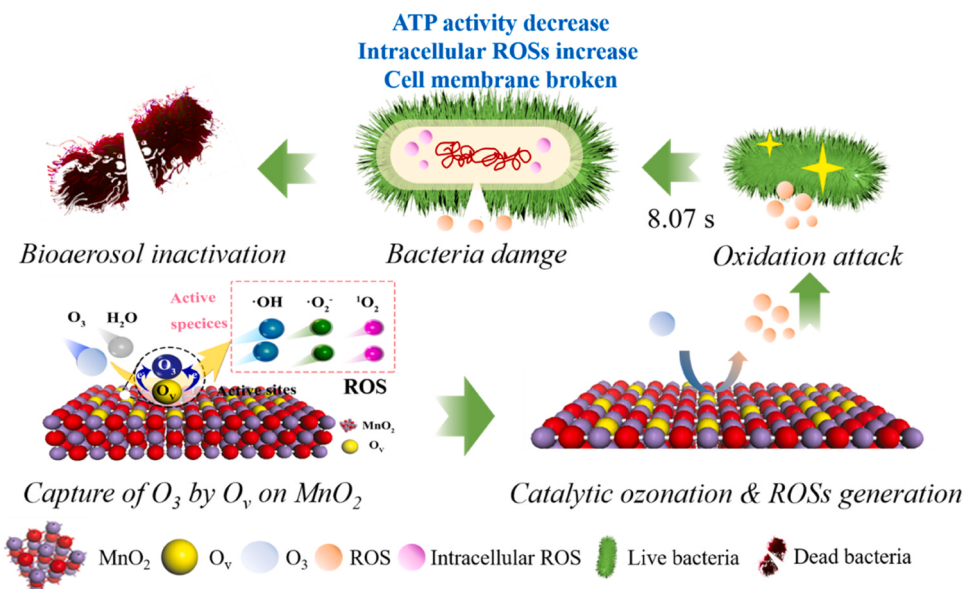


Fig. 6. Illumination of proposed inactivation mechanisms of the MN/O<sub>3</sub> system.

the work reported in this paper.

#### Data availability

No data was used for the research described in the article.

#### Acknowledgments

This work was supported by the National Natural Science Foundation of China (U1901210 and 42207112) and the National Key Research and Development Project (2023YFC3708204 and 2023YFC3708202).

#### Appendix A. Supporting information

Supplementary data associated with this article can be found in the online version at [doi:10.1016/j.apcatb.2023.123675](https://doi.org/10.1016/j.apcatb.2023.123675).

#### References

- [1] W. Xie, Y. Li, W. Bai, J. Hou, T. Ma, X. Zeng, L. Zhang, T. An, The source and transport of bioaerosols in the air: a review, *Front. Env. Sci. Eng.* 15 (2021) 44.
- [2] C.H. Xu, J.M. Chen, Z.K. Wang, H. Chen, H. Feng, L.J. Wang, Y.N. Xie, Z.Z. Wang, X.N. Ye, H.D. Kan, Z.H. Zhao, A. Mellouki, Diverse bacterial populations of PM2.5 in urban and suburb Shanghai, China, *Front. Env. Sci. Eng.* 15 (2021) 37.
- [3] W. Meng, G. Shen, H. Shen, Y. Chen, J. Ma, J. Liu, H. Cheng, J. Hu, Y. Wan, S. Tao, Source contributions and drivers of physiological and psychophysical cobenefits from major air pollution control actions in North China, *Environ. Sci. Technol.* 56 (2022) 2225–2235.
- [4] P.U. Rasmussen, K. Uhrbrand, M.D. Bartels, H. Neustrup, D.G. Karottki, U. Bultmann, A.M. Madsen, Occupational risk of exposure to methicillin-resistant *Staphylococcus aureus* (MRSA) and the quality of infection hygiene in nursing homes, *Front. Env. Sci. Eng.* 15 (2021) 41.
- [5] M.A. Jahne, S.W. Rogers, T.M. Holsen, S.J. Grimberg, I.P. Ramler, S. Kim, Bioaerosol deposition to food crops near manure application: quantitative microbial risk assessment, *J. Environ. Qual.* 45 (2016) 666–674.
- [6] W. Eduard, D. Heederik, C. Duchaine, B.J. Green, Bioaerosol exposure assessment in the workplace: the past, present and recent advances, *J. Environ. Monit.* 14 (2012) 334–339.
- [7] Y. Li, X. Huang, I.T. Yu, T.W. Wong, H. Qian, Role of air distribution in SARS transmission during the largest nosocomial outbreak in Hong Kong, *Indoor Air* 15 (2005) 83–95.
- [8] K. Lin, L.C. Marr, Aerosolization of Ebola virus surrogates in wastewater systems, *Environ. Sci. Technol.* 51 (2017) 2669–2675.
- [9] L. Morawska, J. Cao, Airborne transmission of SARS-CoV-2: the world should face the reality, *Environ. Int.* 139 (2020) 105730.
- [10] C. Yan Suen, Y. Tak Lai, K. Hei Lui, Y. Li, H. Hoi Ling Kwok, Q. Chang, J. Hong Lee, W. Han, X. Yang, Z. Yang, Z. Mo, P. Kin Shing Wong, A. Chi Tat Leung, J. Kai Cho Kwan, K. Lun Yeung, Viricidal, bactericidal, and sporicidal multilevel antimicrobial HEPA-ClO<sub>2</sub> filter for air disinfection in a palliative care facility, *Chem. Eng. J.* 433 (2022) 134115.
- [11] D.M. Costa, L.K.O. Lopes, H. Hu, A.F.V. Tipple, K. Vickery, Alcohol fixation of bacteria to surgical instruments increases cleaning difficulty and may contribute to sterilization inefficacy, *Am. J. Infect. Control* 45 (2017) e81–e86.
- [12] L. Peng, H. Wang, Y. Wang, G. Li, T. An, Photocatalytic inactivation technologies for bioaerosols: advances and perspective, *EES Catal.* (2023), [https://doi.org/10.1039/D1039EY00179B](https://doi.org/10.1039/D1039/D1039EY00179B).
- [13] L. Peng, H. Wang, G. Li, W. Zhang, Z. Liang, T. An, Photocatalytic inactivation of airborne bacteria onto g-C<sub>3</sub>N<sub>4</sub>/TiO<sub>2</sub>/Ni-polydopamine/Ni bifunctional coupling filter with non-size dependent capture effect, *Appl. Catal. B: Environ.* 329 (2023) 122580.
- [14] K.P. Yu, G.W. Lee, S.Y. Lin, C.P. Huang, Removal of bioaerosols by the combination of a photocatalytic filter and negative air ions, *J. Aerosol Sci.* 39 (2008) 377–392.
- [15] R.E. Barnewall, W.E. Bischoff, Removal of SARS-CoV-2 bioaerosols using ultraviolet air filtration, *Infect. Cont. Hosp. Ep.* 42 (2021) 1014–1015.
- [16] M. Yao, G. Mainelis, H.R. An, Inactivation of microorganisms using electrostatic fields, *Environ. Sci. Technol.* 39 (2005) 3338–3344.
- [17] M. Sharma, J.B. Hudson, Ozone gas is an effective and practical antibacterial agent, *Am. J. Infect. Control* 36 (2008) 559–563.
- [18] X. Lu, J. Hong, L. Zhang, O.R. Cooper, M.G. Schultz, X. Xu, T. Wang, M. Gao, Y. Zhao, Y. Zhang, Severe surface ozone pollution in China: a global perspective, *Environ. Sci. Technol. Lett.* 5 (2018) 487–494.
- [19] M. Alimohammadi, M. Naderi, Effectiveness of ozone gas on airborne virus inactivation in enclosed spaces: a review study, *Ozone-Sci. Eng.* 43 (2021) 21–31.
- [20] V.K. Sharma, N.J.D. Graham, Oxidation of amino acids, peptides and proteins by ozone: a review, *Ozone-Sci. Eng.* 32 (2010) 81–90.
- [21] L.R.C. Costa, L.A. Feris, Use of ozonation technology to combat viruses and bacteria in aquatic environments: problems and application perspectives for SARS-CoV-2, *Environ. Technol.* 44 (2023) 2490–2502.
- [22] P. Levif, S. Larocque, J. Séguin, M. Moisan, J. Barbeau, Inactivation of bacterial spores on polystyrene substrates pre-exposed to dry gaseous ozone: mechanisms and limitations of the process, *Ozone-Sci. Eng.* 43 (2020) 112–126.
- [23] G. Moccia, F. De Caro, C. Pironi, G. Boccia, M. Capunzo, A. Borrelli, O. Motta, Development and improvement of an effective method for air and surfaces disinfection with ozone gas as a decontaminating agent, *Medicina* 56 (2020) 578.
- [24] C. Liu, R. Chen, F. Sera, A.M. Vicedo-Cabrera, Y. Guo, S. Tong, E. Lavigne, P. M. Correa, N.V. Ortega, S. Achilleos, D. Roye, J.J. Jaakkola, N. Ryti, M. Pascal, A. Schneider, S. Breitner, A. Entezari, F. Mayvaneh, R. Raz, Y. Honda, M. Hashizume, C.F.S. Ng, V. Gaio, J. Madiureira, I.-H. Holobaca, A. Tobias, C. Íñiguez, Y.L. Guo, S.-C. Pan, P. Masselot, M.L. Bell, A. Zanobetti, J. Schwartz, A. Gasparini, H. Kan, Interactive effects of ambient fine particulate matter and ozone on daily mortality in 372 cities: two stage time series analysis, *BMJ* 383 (2023) e075203.
- [25] E.I. Epelle, A. Macfarlane, M. Cusack, A. Burns, N. Amaeze, W. Mackay, M. Yaseen, The impact of gaseous ozone penetration on the disinfection efficiency of textile materials, *Ozone-Sci. Eng.* 45 (2023) 232–246.
- [26] C. Dong, J.J. Yang, L.H. Xie, G. Cui, W.H. Fang, J.R. Li, Catalytic ozone decomposition and adsorptive VOCs removal in bimetallic metal-organic frameworks, *Nat. Commun.* 13 (2022) 4991.
- [27] W. Hong, Y. Liu, T. Zhu, H. Wang, Y. Sun, F. Shen, X. Li, Promoting the catalytic ozonation of toluene by introducing SO<sub>4</sub><sup>2-</sup> into the alpha-MnO<sub>2</sub>/ZSM-5 catalyst to tune both oxygen vacancies and acid sites, *Environ. Sci. Technol.* 56 (2022) 15695–15704.

[28] Q. Yu, H. Pan, M. Zhao, Z. Liu, J. Wang, Y. Chen, M. Gong, Influence of calcination temperature on the performance of Pd-Mn/SiO<sub>2</sub>-Al<sub>2</sub>O<sub>3</sub> catalysts for ozone decomposition, *J. Hazard. Mater.* 172 (2009) 631–634.

[29] Z.P. Hao, D.Y. Cheng, Y. Guo, Y.H. Liang, Supported gold catalysts used for ozone decomposition and simultaneous elimination of ozone and carbon monoxide at ambient temperature, *Appl. Catal. B: Environ.* 33 (2001) 217–222.

[30] X. Li, J. Ma, H. He, Tuning the chemical state of silver on Ag-Mn catalysts to enhance the ozone decomposition performance, *Environ. Sci. Technol.* 54 (2020) 11566–11575.

[31] C. Mansas, J. Mendret, S. Brosillon, A. Ayral, Coupling catalytic ozonation and membrane separation: a review, *Sep. Purif. Technol.* 236 (2020) 116221.

[32] Q. Shao, S. Wei, X. Hu, H. Dong, T. Wen, L. Gao, C. Long, Tuning the micro-coordination environment of Al in dealumination Y zeolite to enhance electron transfer at the Cu-Mn oxides interface for highly efficient catalytic ozonation of toluene at low temperatures, *Environ. Sci. Technol.* 56 (2022) 15449–15459.

[33] R. Yang, Y. Fan, R. Ye, Y. Tang, X. Cao, Z. Yin, Z. Zeng, MnO<sub>2</sub>-based materials for environmental applications, *Adv. Mater.* 33 (2021) 2004862.

[34] C. He, Y. Wang, Z. Li, Y. Huang, Y. Liao, D. Xia, S. Lee, Facet engineered alpha-MnO<sub>2</sub> for efficient catalytic ozonation of odor CH<sub>3</sub>SH: oxygen vacancy-induced active centers and catalytic mechanism, *Environ. Sci. Technol.* 54 (2020) 12771–12783.

[35] J. Huang, S. Zhong, Y. Dai, C.C. Liu, H. Zhang, Effect of MnO<sub>2</sub> phase structure on the oxidative reactivity toward bisphenol a degradation, *Environ. Sci. Technol.* 52 (2018) 11309–11318.

[36] X. Wan, K. Shi, H. Li, F. Shen, S. Gao, X. Duan, S. Zhang, C. Zhao, M. Yu, R. Hao, W. Li, G. Wang, M. Peressi, Y. Feng, W. Wang, Catalytic ozonation of polluter benzene from -20 to >50 degrees C with high conversion efficiency and selectivity on mullite YMn<sub>2</sub>O<sub>5</sub>, *Environ. Sci. Technol.* 57 (2023) 8435–8445.

[37] B. Zhang, Y. Shen, B. Liu, J. Ji, W. Dai, P. Huang, D. Zhang, G. Li, R. Xie, H. Huang, Boosting ozone catalytic oxidation of toluene at room temperature by using hydroxyl-mediated MnO<sub>x</sub>/Al<sub>2</sub>O<sub>3</sub> catalysts, *Environ. Sci. Technol.* 57 (2023) 7041–7050.

[38] A. Wang, J. Guan, L. Zhang, H. Wang, G. Ma, G. Fan, W. Tang, N. Han, Y. Chen, In situ synthesis of monolithic Cu<sub>2</sub>O-CuO/Cu catalysts for effective ozone decomposition, *J. Phys. Chem. C.* 126 (2022) 317–325.

[39] A. Zhang, R. Zhao, L. Hu, R. Yang, S. Yao, S. Wang, Z. Yang, Y.M. Yan, Adjusting the coordination environment of Mn enhances supercapacitor performance of MnO<sub>2</sub>, *Adv. Energy Mater.* 11 (2021) 2101412.

[40] X. Wang, Y. Li, Selected-control hydrothermal synthesis of  $\alpha$ - and  $\beta$ -MnO<sub>2</sub> single crystal nanowires, *J. Am. Chem. Soc.* 124 (2002) 2880–2881.

[41] H. Wang, L. Peng, G. Li, W. Zhang, Z. Liang, H. Zhao, T. An, Photocatalytic ozonation inactivation of bioaerosols by NiFeOOH nanosheets in situ grown on nickel foam, *Appl. Catal. B: Environ.* 324 (2023) 122273.

[42] G. Zhu, W. Zhu, Y. Lou, J. Ma, W. Yao, R. Zong, Y. Zhu, Encapsulate alpha-MnO<sub>2</sub> nanofiber within graphene layer to tune surface electronic structure for efficient ozone decomposition, *Nat. Commun.* 12 (2021) 4152.

[43] G. Zhu, J. Zhu, W. Jiang, Z. Zhang, J. Wang, Y. Zhu, Q. Zhang, Surface oxygen vacancy induced  $\alpha$ -MnO<sub>2</sub> nanofiber for highly efficient ozone elimination, *Appl. Catal. B: Environ.* 209 (2017) 729–737.

[44] J. Jenkins, J. Mantell, C. Neal, A. Gholinia, P. Verkade, A.H. Nobbs, B. Su, Antibacterial effects of nanopillar surfaces are mediated by cell impedance, penetration and induction of oxidative stress, *Nat. Commun.* 11 (2020) 1626.

[45] E.I. Epelle, A. Macfarlane, M. Cusack, A. Burns, N. Amaze, W. Mackay, M. Yaseen, The impact of gaseous ozone penetration on the disinfection efficiency of textile materials, *Ozone-Sci. Eng.* 45 (2023) 232–246.

[46] E.N. Paddy, O.O.D. Afolabi, M. Sohail, Toilet plume bioaerosols in health care and hospitality settings: a systematic review, *Am. J. Infect. Control* 51 (2023) 324–333.

[47] S. Zhang, Z. Liang, X. Wang, Z. Ye, G. Li, T. An, Bioaerosols in an industrial park and the adjacent houses: Dispersal between indoor/outdoor, the impact of air purifier, and health risk reduction, *Environ. Int.* 172 (2023) 107778.

[48] A. Oppiger, S. Rusca, N. Charriere, T. Vu Duc, P.O. Droz, Assessment of bioaerosols and inhalable dust exposure in Swiss sawmills, *Ann. Occup. Hyg.* 49 (2005) 385–391.

[49] A.I. Gomes, J.C. Santos, V.J.P. Vilar, R.A.R. Boaventura, Inactivation of Bacteria *E. coli* and photodegradation of humic acids using natural sunlight, *Appl. Catal. B: Environ.* 88 (2009) 283–291.

[50] G. Zhu, J. Zhu, W. Li, W. Yao, R. Zong, Y. Zhu, Q. Zhang, Tuning the K<sup>+</sup> concentration in the tunnels of  $\alpha$ -MnO<sub>2</sub> to increase the content of oxygen vacancy for ozone elimination, *Environ. Sci. Technol.* 52 (2018) 8684–8692.

[51] T. Ren, M. Yin, S. Chen, C. Ouyang, X. Huang, X. Zhang, Single-atom Fe-N<sub>4</sub> sites for catalytic ozonation to selectively induce a nonradical pathway toward wastewater purification, *Environ. Sci. Technol.* 57 (2023) 3623–3633.

[52] L. Zhang, J. Yang, A. Wang, S. Chai, J. Guan, L. Nie, G. Fan, N. Han, Y. Chen, High performance ozone decomposition spinel (Mn<sub>3</sub>Co)<sub>3</sub>O<sub>4</sub> catalyst accelerating the rate-determining step, *Appl. Catal. B: Environ.* 303 (2022) 120927.

[53] J. Jin, Y. Liu, X. Zhao, H. Liu, S. Deng, Q. Shen, Y. Hou, H. Qi, X. Xing, L. Jiao, J. Chen, Annealing in argon universally upgrades the Na-storage performance of Mn-based layered oxide cathodes by creating bulk oxygen vacancies, *Angew. Chem.* 62 (2023) e202219230.

[54] J. Miao, J. Song, J. Lang, Y. Zhu, J. Dai, Y. Wei, M. Long, Z. Shao, B. Zhou, P.J. J. Alvarez, L. Zhang, Single-atom MnN<sub>5</sub> catalytic sites enable efficient peroxyomonosulfate activation by forming highly reactive Mn(IV)-Oxo species, *Environ. Sci. Technol.* 57 (2023) 4266–4275.

[55] Z.H. Huang, Y. Song, D.Y. Feng, Z. Sun, X. Sun, X.X. Liu, High mass loading MnO<sub>2</sub> with hierarchical nanostructures for supercapacitors, *ACS Nano* 12 (2018) 3557–3567.

[56] W.V. Glassey, R. Hoffmann, A molecular orbital study of surface-adsorbate interactions during the oxidation of CO on the Pt(111) surface, *Surf. Sci.* 475 (2001) 47–60.

[57] X.X. Yang, Y. Tian, S. Mukherjee, K. Li, X.Y. Chen, J.Q. Lv, S. Liang, L.K. Yan, G. Wu, H.Y. Zang, Constructing oxygen vacancies via engineering heterostructured Fe<sub>3</sub>C/Fe<sub>3</sub>O<sub>4</sub> catalysts for electrochemical ammonia synthesis, *Angew. Chem. Int. Ed.* 62 (2023) e202304797.

[58] R. Liu, S.J. Liu, H. Ding, D. Zhao, J.F. Fu, Y.X. Zhang, W.C. Huo, G. Li, Unveiling the role of atomically dispersed active sites over amorphous iron oxide supported Pt catalysts for complete catalytic ozonation of toluene at low temperature, *Ind. Eng. Chem. Res.* 60 (2021) 3881–3892.

[59] K.I. Ishibashi, A. Fujishima, T. Watanabe, K. Hashimoto, Generation and deactivation processes of superoxide formed on TiO<sub>2</sub> film illuminated by very weak UV light in air or water, *J. Phys. Chem. B* 104 (20) (2000) 4934–4938.

[60] L.H. Peng, H.Y. Wang, G.Y. Li, Z.S. Liang, W.P. Zhang, W.N. Zhao, T.C. An, Bioinspired artificial spider silk photocatalyst for the high-efficiency capture and inactivation of bacteria aerosols, *Nat. Commun.* 14 (2023) 2412.

[61] L. Long, J. Zhao, L. Yang, M. Fu, J. Wu, B. Huang, D. Ye, Room temperature catalytic ozonation of toluene over MnO<sub>2</sub>/Al<sub>2</sub>O<sub>3</sub>, *Chin. J. Catal.* 32 (2011) 904–916.

[62] H. Wang, Z. Huang, Z. Jiang, Z. Jiang, Y. Zhang, Z. Zhang, W. Shangguan, Trifunctional C@MnO catalyst for enhanced stable simultaneously catalytic removal of formaldehyde and ozone, *ACS Catal.* 8 (2018) 3164–3180.

[63] W. Qu, Z. Tang, S. Tang, H. Wen, J. Fang, Q. Lian, D. Shu, C. He, Cation substitution induced d-band center modulation on cobalt-based spinel oxides for catalytic ozonation, *Adv. Funct. Mater.* 33 (2023) 2301677.

[64] H.L. Yin, G.Y. Li, X.F. Chen, W.J. Wang, P.K. Wong, H.J. Zhao, T.C. An, Accelerated evolution of bacterial antibiotic resistance through early emerged stress responses driven by photocatalytic oxidation, *Appl. Catal. B: Environ.* 269 (2020) 118829.